Research Article

Nano Research
2023, 16(4): 5226–5236

ISSN 1998-0124 CN 11-5974/O4
https://doi.org/10.1007/s12274-022-5139-z

Reductive damage induced autophagy inhibition for tumor therapy

Yuqian Wang[1,2,3,§], Yingjian Huang[3,§], Yu Fu[4], Zhixiong Guo[2], Da Chen[2], Fangxian Cao[2], Qi Ye[5], Qiqi Duan[3], Meng Liu[3], Ning Wang[3], Dan Han[1], Chaoyi Qu[6], Zhimin Tian[2] (✉), Yongquan Qu[2] (✉), and Yan Zheng[1] (✉)

[1] *Department of Dermatology, the First Affiliated Hospital of Xi'an Jiaotong University, Xi'an 710061, China*
[2] *Key Laboratory of Special Functional and Smart Polymer Materials of Ministry of Industry and Information Technology, School of Chemistry and Chemical Engineering, Northwestern Polytechnical University, Xi'an 710072, China*
[3] *Department of Dermatology, the Second Affiliated Hospital, School of Medicine, Xi'an Jiaotong University, Xi'an 710004, China*
[4] *School of Chemical Engineering and Technology, Shaanxi Key Laboratory of Energy Chemical Process Intensification, Xi'an Jiaotong University, Xi'an 710049, China*
[5] *Department of Urology, the First Affiliated Hospital of Xi'an Jiaotong University, Xi'an 710061, China*
[6] *Xi'an People's Hospital (Xi'an Fourth Hospital), Shaanxi Eye Hospital, Affiliated Guangren Hospital, School of Medicine, Xi'an Jiaotong University, Xi'an 710004, China*
[§] *Yuqian Wang and Yingjian Huang contributed equally to this work.*

Received: 27 July 2022 / **Revised:** 27 September 2022 / **Accepted:** 2 October 2022

ABSTRACT

Numerous therapeutic anti-tumor strategies have been developed in recent decades. However, their therapeutic efficacy is reduced by the intrinsic protective autophagy of tumors. Autophagy plays a key role in tumorigenesis and tumor treatment, in which the overproduction of reactive oxygen species (ROS) is recognized as the direct cause of protective autophagy. Only a few molecules have been employed as autophagy inhibitors in tumor therapy to reduce protective autophagy. Among them, hydroxychloroquine is the most commonly used autophagy inhibitor in clinics, but it is severely limited by its high therapeutic dose, significant toxicity, poor reversal efficacy, and nonspecific action. Herein, we demonstrate a reductive-damage strategy to enable tumor therapy by the inhibition of protective autophagy via the catalytic scavenging of ROS using porous nanorods of ceria (PN-CeO_2) nanozymes as autophagy inhibitor. The antineoplastic effects of PN-CeO_2 were mediated by its high reductive activity for intratumoral ROS degradation, thereby inhibiting protective autophagy and activating apoptosis by suppressing the activities of phosphatidylinositide 3-kinase/protein kinase B and p38 mitogen-activated protein kinase pathways in human cutaneous squamous cell carcinoma. Further investigation highlighted PN-CeO_2 as a safe and efficient anti-tumor autophagy inhibitor. Overall, this study presents a reductive-damage strategy as a promising anti-tumor approach that catalytically inhibits autophagy and activates the intrinsic antioxidant pathways of tumor cells and also shows its potential for the therapy of other autophagy-related diseases.

KEYWORDS

CeO_2, reductive damage, autophagy inhibitor, tumor therapy, reactive oxygen species

1 Introduction

The generation of reactive oxygen species (ROS) and subsequent oxidative damage in a tumor environment (TME) is the dominant mechanism of contemporary tumor treatment strategies, including chemotherapy [1–4], radiotherapy [5], photodynamic therapy [6, 7], and photothermal and catalytic therapy [8–18]. However, elevated intratumoral ROS levels can also increase tumor cell survival and proliferation, especially through the activation of protective autophagy [19, 20]. This self-protective mechanism is regarded as a major protective pathway that defends cells against inflammation, degenerative diseases, and infection (e.g., SARS-CoV-2 and HIV) [21–24]. Unfortunately, under high levels of cellular ROS, autophagy may be hijacked as a survival mechanism by tumor cells that resist therapeutic challenges. High-level protective autophagy of tumor cells enhances their resistance to drug therapy and improves their survival under nutrient-limiting and low-oxygen conditions [25–30]. Moreover, autophagy and apoptosis are mutually exclusive cellular processes, and the inhibition of autophagy can hinder the degradation of damaged mitochondria, promote subsequent apoptosis, and inhibit the survival of cancer cells [31, 32]. Therefore, suppressing protective autophagy is an effective strategy to attenuate the progression of a tumor [25, 33–36].

Various nanomaterials (nanomicelles, iron oxide, gold, C60, $CuFe_2O_4$, etc.) that interfere with the autophagy process are used in tumor treatments; however, higher efficacy is generally achieved by combined therapies involving nanomaterials and an autophagy inhibitor, such as chloroquine or hydroxychloroquine (HCQ) [29, 31, 33–37]. HCQ, the only clinically approved autophagy inhibitor, has been shown to have anti-tumor effects by inhibiting autophagy and subsequently inducing tumor cell apoptosis [34, 38, 39]. However, its practical application in cancer treatment faces enormous challenges owing to its very high therapeutic dose

Address correspondence to Yan Zheng, zhengyan2018@xjtu.edu.cn; Yongquan Qu, yongquan@nwpu.edu.cn; Zhimin Tian, zhimintian@nwpu.edu.cn

(1,200 mg/day) and toxicity to human beings, potentially inducing myocardial infarction, heart failure, chronic renal failure, visual distortion, and even complete loss of sight [29, 38, 39]. Considering this, there is significant demand for next-generation autophagy inhibitors with high biosafety, specific drug distribution, high bioavailability, and enhanced permeability and retention. As ROS is closely associated with autophagy, natural antioxidants have previously been considered as potential therapeutic agents to inhibit protective autophagy [40, 41]. Unfortunately, the utilization of such natural antioxidants *in vivo* and in clinical trials is seriously restricted by their unfavorable pharmacokinetics, including poor solubility in water, low bioavailability, limited ROS scavenging ability, and susceptibility to degradation in TME [42, 43].

Compared with natural antioxidants, antioxidative nanozymes have demonstrated ROS scavenging capabilities with features of scalable synthesis, facile storage, high structural stability, and prolonged circulation time [44–48]. Among these artificial antioxidants, nanoceria is a classic nanozyme with excellent catalytic activity for the degradation of various ROS including hydrogen peroxide, hydroxyl radicals, and superoxide anions owing to its reversible Ce^{3+}/Ce^{4+} redox pair associated with the structural defects of oxygen vacancies [44–46, 49–55]. The abundance of oxygen vacancies indexed by the surface Ce^{3+}/Ce^{4+} ratio has been shown to be correlated with its superoxide dismutase (SOD)- and catalase (CAT)-like activities [53–55]. Therefore, nanoceria with controllable morphologies and surface physicochemical properties are increasingly being evaluated as potential candidates for the treatment of a large variety of ROS-related diseases, including neurodegenerative diseases, ophthalmopathy, stroke, and inflammation [49–55]. Recently, nanoceria has been employed to reduce excessive and sustained autophagy activation for hepatic fibrosis therapy by scavenging ROS from human hepatic stellate cell line [56]. Similarly, nanoceria shows potential as autophagy regulator for tumor cells, needing further exploration. Furthermore, a majority of tumor-related treatments currently employ ROS damage mechanisms, while therapeutic strategies for tumor reductive damage are rarely reported.

Herein, we demonstrate a catalytic reductive-damage strategy that enables tumor treatment by inhibiting protective autophagy using CeO_2 nanozymes (Scheme 1). Human cutaneous squamous cell carcinoma (cSCC), the most prevalent type of non-melanoma skin cancer with an estimated annual incidence of more than three million cases worldwide, is reported to have a high level of autophagy and is used here as the tumor model for therapy [57]. The highly defective porous nanorods of ceria (PN-CeO_2), used as a reductive nanozyme with high biocompatibility, efficiently catalyzed the degradation of the harmful intratumoral ROS. Systematic *in vitro* and *in vivo* investigations demonstrated that

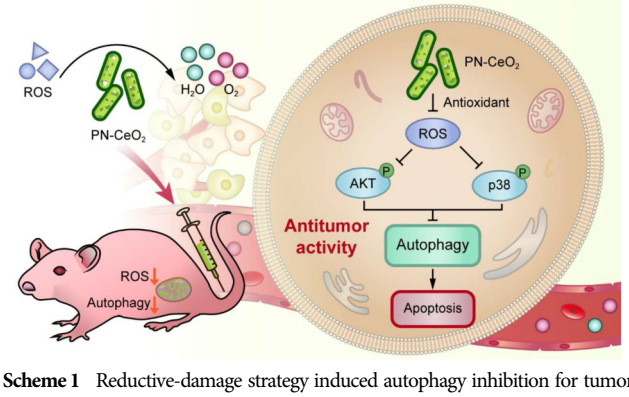

Scheme 1 Reductive-damage strategy induced autophagy inhibition for tumor therapy.

PN-CeO_2 nanozymes effectively attenuated tumor progression by decreasing the intratumor levels of ROS and subsequently inhibiting protective autophagy as a single agent (i.e., without a small molecule autophagy inhibitor). Moreover, in xenograft models for cSCC, the intravenously injected PN-CeO_2 exhibited stable tumor-suppressing effects via the downregulation of protective autophagy and the decreased activities of the phosphatidylinositide 3-kinase/protein kinase B (PI3K/AKT) and p38 mitogen-activated protein kinase (MAPK) pathways [58, 59], with negligible side effects. Therefore, our study developed an effective reductive-damage strategy to inhibit protective autophagy through catalytic ROS consumption and provided a feasible methodology for oncological therapy.

2 Experimental

2.1 Synthesis and characterization of PN-CeO_2

PN-CeO_2 was synthesized through a two-step hydrothermal approach as described in our previous report [50]. Furthermore, the morphology and size of PN-CeO_2 were characterized by transmission electron microscopy (TEM, JEOL JEM-F200), X-ray diffractometer (XRD, Shimadzu, Model 6000) in the 2θ range 10°–90°, and X-ray photoelectron spectrometry (XPS, Thermo Electron Model K-Alpha). The surface areas of the catalysts were derived from nitrogen physisorption (Quantachrome) based on the Brunauer–Emmet–Teller (BET) method. Electron paramagnetic resonance (EPR) spectra were recorded using a Bruker EMXplus spectrometer. The concentrations of Ce in various organs were measured by inductively coupled plasma-mass spectrometry (ICP-MS, PerkinElmer).

2.2 CAT-like activity assay

The CAT-like activity of PN-CeO_2 was determined by a hydrogen peroxide assay kit (Beyotime) according to the manufacture's protocol. Initially, 10 μL of the freshly prepared H_2O_2 aqueous solution (0.1 M) was added to 90 μL PN-CeO_2 suspensions of various concentrations (5, 10, 25, 50, and 100 μg/mL in saline solution) and then incubated for 10 min at 37 °C. Afterwards, 50 μL of the working solution was added to each sample. The mixture was allowed to react at 37 °C for 15 min before the absorbance was measured at 560 nm (Tecan, Infinite E Plex).

2.3 SOD-like activity assay

The SOD-like activity of PN-CeO_2 was determined by a SOD activity kit (Beyotime), according to the manufacturer's protocol. First, 10 μL of PN-CeO_2 suspended in saline solution with various concentrations (5, 10, 25, 50, and 100 μg/mL) and 160 μL of working solution were mixed and added to a 96-well plate. Afterwards, 20 μL of reaction starter solution was added to the mixtures, which were then incubated for 10 min at 37 °C. Then, the absorption peak at 450 nm was detected by using a microplate reader (Tecan, Infinite E Plex).

2.4 Cell culture

The human cSCC cell line SCL-1 (Boukamp et al., 1982) and keratinocyte cell line HaCaT cells were purchased from Beijing Beinachuanglian Biotechnology Research Institute (Beijing, China, http://www.bnbio.com). Human cervical carcinoma cell line HeLa, human colon cancer cell line HCT-116, human prostate cancer cell line PC-3, human lung adenocarcinoma cell line A549, and human hepatocellular carcinoma cell line HepG2 were purchased from ATCC and presented by the Center for Mitochondrial Biology and Medicine of Xi'an Jiaotong University. The cells were cultured in high glucose Dulbecco's modified Eagle

medium (DMEM) supplemented with 10% heat-inactivated fetal bovine serum (Biological Industries) and 1% antibiotics (penicillin-streptomycin) at 37 °C in a humidified incubator containing 5% CO_2.

2.5 Cellular uptake assay

SCL-1 cells were cultured and treated with PN-CeO_2 at a concentration of 100 μg/mL for 24 h. They were then fixed overnight in a paraformaldehyde solution (2.5% phosphate-buffered saline (PBS)) at 4 °C and subsequently surface-embedded in epoxy resin. Transverse thin-sections were cut and transferred to a carbon-coated grid, and the samples were viewed by TEM at an acceleration voltage of 80 kV (Hitachi HT7650).

2.6 Cell proliferation assay

Cell proliferation was assessed using a 3-(4,5-dimethylthiazol-2-yl)-2,5-diphenyltetrazolium bromide (MTT) assay. Firstly, 3×10^3 cells/well were plated in 96-well plates, which were then incubated at 37 °C under 5% CO_2. After 24 h of incubation, the cells were treated with various concentrations of PN-CeO_2 or HCQ (Sigma-Aldrich). At different time, a 10% volume of MTT solution (5 mg/mL) was added to each well and incubated at 37 °C for 4 h. Then, 200 μL of dimethyl sulfoxide was added after removing the medium, to dissolve the formazan crystals. The optical density value was measured at a wavelength of 490 nm using a microplate spectrophotometer (Multiskan Ascent, Thermo Fisher Scientific Inc., Waltham, MA, USA). Cell viability was expressed as a percentage relative to that of the control. The mean values of the readings from three independent experiments were plotted for each time point. Five replicate wells were used for each analysis.

2.7 ROS detection

SCL-1 cells (4×10^4 mL^{-1}) were plated in six-well plates overnight for adherence. After pre-incubation, the cells were treated with 0, 50, or 100 μg/mL of PN-CeO_2 for 48 h. For fluorescent image detection, the cells were incubated with 2',7'-dichlorofluorescein diacetate (DCFH-DA) followed by 4',6-diamidino-2-phenylindole (DAPI) and then imaged with confocal laser scanning microscopy (Nikon Eclipse C1). For quantitative analysis, the supernatant was removed, and the cells were trypsinized with EDTA-free trypsinogen and incubated with DCFH-DA (10 μM) in the dark at 37 °C for 30 min. Afterwards, the cells were washed twice in PBS and analyzed using a flow cytometer (AECA NovoCyte from Agilent, USA) at 490 nm excitation and 525 nm emission. The production of ROS in tumor tissues was measured using dihydroethidium staining as previously described [42].

2.8 Detection of SOD and glutathione peroxidase (GSH-Px) levels

SCL-1 cells (6×10^4 mL^{-1}) were seeded into six-well plates in 2 mL of DMEM and preincubated for 24 h at 37 °C. After preincubation, the cells were treated with PN-CeO_2 for 48 h. Subsequently, the SCL-1 cells were washed thrice with cold PBS and ultrasonically lysed. The cell homogenates were centrifuged at 12,000 rpm and 4 °C for 10 min, and the supernatants were collected for analysis. The SOD and GSH-Px levels were assayed using commercial clinical diagnosis kits according to the manufacturer's instructions (Nanjing Jiancheng Bioengineering Institute). The tumor tissue lysis method was the same as that for the SCL-1 cells.

2.9 Western blot

Protein expression levels of SCL-1 cell lysates were analyzed by standard western blot protocol. The primary antibodies used in the study were AKT1/2/3 (sc-81434), p-AKT (sc-514032), p38 MAPK (sc-7972), p-p38 MAPK (sc-166182), nuclear factor erythroid 2-related factor 2 (Nrf2) (sc-365949), BECN1/Beclin1 (sc-48341), light chain 3B (LC3B) (sc-271625), phosphorylated p62 (p-p62) (ab211324), and Actin (66009-1-lg).

2.10 RNA isolation and quantitative real-time polymerase chain reaction (qRT-PCR)

The total RNA was extracted using Trizol Reagent (15596026, Invitrogen) according to the manufacturer's instructions. qRT-PCR was performed on a real-time PCR system (Eppendorf, Germany) using SYBR Green Premix Ex Taq (TaKaRa Bio). The primer oligonucleotide sequences were as follows: β-actin: forward 5'-CCACACCTTCTACAATGAGC-3', reverse 5'-GGTCTCAAACATGATCTGGG-3'; Nrf2: forward 5'-TTCAGCAGCATCCTCTCCACAG-3', reverse 5'- GCATGCTGTTGCTGATACTGG-3'; SOD1: forward 5'-CTAGCGAGTTATGGCGAC-3', reverse 5'-CATTGCCCAAGTCTCCAAC-3'; SOD2: forward 5'-GACACTTACAAATTGCTGCTTGTCC-3', reverse 5'-CTTTCAGTTACATTCTCCCAGTTG-3'; GPx: forward 5'-CGCCAAGAACGAAGAGATTC-3', reverse 5'-CAACATCGTTGCGACACAC-3'; CAT: forward 5'-CAGAGGAAACGTCTGTGTGAGAC-3', reverse 5'-CAAGTGTCCGGACTGCAC-3'; Hemeoxygenase 1 (HO-1): forward 5'-CAGGCAGAGAATGCTGAG-3', reverse 5'-GCTTCACATAGCGCTGCA-3'; NAD(P)H quinone dehydrogenase 1 (NQO-1): forward 5'-TGGCTAGGTATCATTCAACTC-3', reverse 5'-CCTTAGGGCAGGTAGATTCAG-3'; Glutathione S-Transferase Mu 4 (GSTM4): forward 5'-GCCAGTGGCTGAATGAAAAA-3', reverse 5'-CCAGCTGCATATGGTTGTCC-3'; Glutathione s-transferase alpha 4 (GSTA4): forward 5'-GGAGTCCGTGAGATGGGTTT-3', reverse 5'-TGTTGGAACAGCAGGTGGTT-3'; Glutamate-cysteine ligase catalytic subunit (GCLC): forward 5'-TACGGAGGAACAATGTCCGA-3', reverse 5'-CAGTGTGAACCCAGGACAGC-3'; Glutamate-cysteine ligase modifier subunit (GCLM): forward 5'-GCTGTATCAGTGGGCACAGG-3', reverse 5'-TGACCGAATACCGCAGTAGC-3'. β-actin was used as an internal control, and the data were analyzed using the $2^{-\Delta\Delta C_T}$ method.

2.11 Cell apoptosis analysis

The apoptosis after various treatments was analyzed by flow cytometry. SCL-1 cells were plated in six-well plates and incubated under various conditions for 48 h. The apoptotic cells were examined by using an FITC Annexin V apoptosis detection kit (BD Biosciences) according to the manufacturer's instructions. Apoptotic cells were detected using a flow cytometry (AECA NovoCyte from Agilent, USA). Terminal deoxynucleotidyl transferase-mediated dUTP-biotin nick end-labeling (TUNEL) was conducted using a commercially available kit (Servicebio). SCL-1 cells were seeded on glass coverslips in six-well plates overnight and then treated with PN-CeO_2 for 48 h. The cells were then fixed in a 4% paraformaldehyde, rinsed with PBS, and then permeabilized by 0.1% Triton X-100 for Cy3 end-labeling of the fragmented DNA. The Cy3-labeled TUNEL-positive cells were imaged under a confocal microscope (Nikon Eclipse C1) with 490 nm excitation and 520 nm emission.

2.12 Animal studies

Female BALB/c/nu nude mice (4–5 weeks old) were purchased from Beijing Vital River Company (License number: SCXK (Jing) 2016-0006). The mice were bred at the animal facilities of Xi'an Jiaotong University under specific pathogen-free conditions in closed-top cages. Six mice were individually inoculated subcutaneously on their right flanks with 5×10^6 SCL-1 cells.

When the tumors reached 50 mm^3, the mice were intravenously injected with the same volume (100 μL) of saline (0.9%, control) or PN-CeO_2 (10 mg/kg). Tumor sizes were measured every 2 days using digital microcalipers, and tumor volumes were calculated as length × width × width/2. After 12 days, the mice were sacrificed, and the tumors were excised for weight, western blot, and histological analyses. All animal protocols were approved by the Institutional Animal Care and Use Committee of Xi'an Jiaotong University.

2.13 Hematoxylin and eosin staining and blood biochemical index

Organ and tumor tissues were washed with cold PBS and fixed in 4% paraformaldehyde for 24 h, dehydrated using a series of graded ethanol, and embedded in paraffin. Tissues were cut into 5 μm thick sections. The fixed sections were deparaffinized and hydrated according to a standard protocol and stained with hematoxylin and eosin (H&E). The H&E-stained sections were scanned using a Hamamatsu digital pathology system, and biochemical analyses were performed using an automated biochemical analyzer (Chemray800, Rayto).

2.14 TUNEL assay of tumor tissues

The TUNEL assays of tumor tissues were conducted using a TUNEL apoptosis assay kit (Servicebio) according to the manufacturer's instructions. Approximately 5 μm thick tumor slices were incubated with proteinase K (20 μg/mL) for 25 min at 37 °C and washed thrice with PBS (pH 7.4). Next, the permeabilization working solution was added and incubated at 25 °C for 20 min. Subsequently, tumor slices were incubated with a TUNEL detection solution at 37 °C for 2 h and washed thrice with PBS. The samples were imaged by confocal laser scanning microscopy (Nikon Eclipse C1) at 490 nm excitation and 520 nm emission.

2.15 Immunofluorescent staining

The tumor tissues were fixed in 4% paraformaldehyde for 24 h and embedded in paraffin. Then, approximately 5 μm thick paraffin-embedded tumor slices were cut and transferred onto a glass slide. After deparaffinization, the slides were immersed in PBS for 20 min at 25 °C and then incubated with primary antibodies overnight at 4 °C. Tumor slices were washed three times with PBS for 5 min each and incubated with Alexa Fluor® 488-conjugated goat anti-mouse IgG (1:500, Servicebio, GB25301) diluted in a blocking buffer for 2 h at 25 °C. After incubation, the tumor slices were washed three times with PBS for 5 min each and left in the PBS with DAPI until imaging. Images were captured by confocal laser scanning microscopy (Nikon Eclipse C1) at 495 nm excitation and 520 nm emission. The primary antibodies used in this study were BECN1/Beclin1 (1:200, Santa, sc-48341), LC3B (1:200, Santa, sc-271625), p-p62 (1:100, ab211324, Abcam), p-AKT (1:200, Santa, sc-514032), p-p38 (1:200, Santa, sc-16182), and casepase-3 (1:200, Santa, sc-56053).

2.16 Statistical analysis

All results were expressed as mean ± standard error of mean (SEM). The statistical analysis was performed using GraphPad Prism 8.0. The Student's *t*-test was used for comparisons between two groups, whereas one-way and two-way analysis of variance (ANOVA) followed by a Dunnett's test were used for comparing three or more groups. $P < 0.05$ was considered statistically significant.

3 Results and discussion

3.1 Preparation and characterization of PN-CeO_2

PN-CeO_2 was synthesized via a two-step hydrothermal method [50]. The shape of the PN-CeO_2 was examined by TEM. As-synthesized PN-CeO_2 presented a porous nanorod-like shape with relatively uniform morphology with an average length, diameter, and pore size of approximately 60, 8, and 2 nm, respectively (Fig. 1(a)). Element mapping images indicated a uniform elemental distribution of Ce and O in the nanorods (Fig. 1(b)). The crystal structure of PN-CeO_2 was identified as a fluorite structure from the XRD pattern (Fig. 1(c)). These results indicate the successful synthesis of PN-CeO_2. As shown in Fig. 1(d), the N_2 adsorption/desorption isotherm of PN-CeO_2 was a typical type IV curve with H1 hysteresis loops, suggesting that the pores were

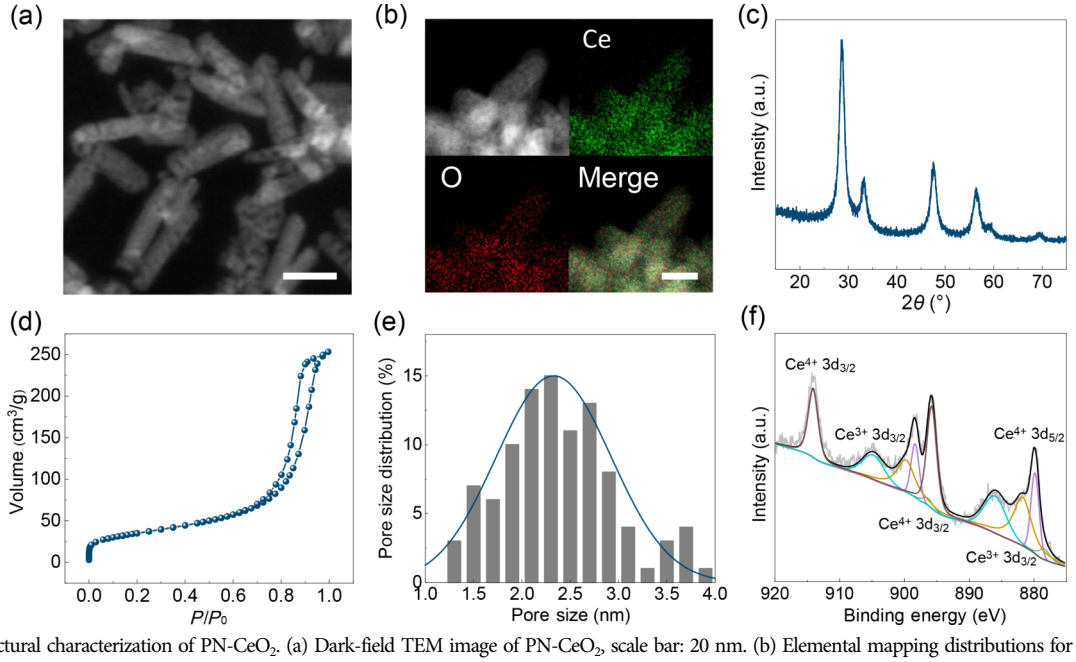

Figure 1 Structural characterization of PN-CeO_2. (a) Dark-field TEM image of PN-CeO_2, scale bar: 20 nm. (b) Elemental mapping distributions for Ce and O and overlap of PN-CeO_2, scale bar: 10 nm. (c) XRD pattern of PN-CeO_2. (d) N_2 adsorption/desorption isotherm of PN-CeO_2. (e) Pore size distribution of PN-CeO_2 measured from dark-field TEM images (100 nanopores). (f) XPS spectrum of PN-CeO_2.

mainly composed of mesopores. The surface area of the PN-CeO_2, as determined by BET analysis, was 123.8 m^2/g. The average pore size derived from dark-field TEM images (Fig. 1(e)) was 2.3 ± 0.5 nm. In general, such a highly porous structure and large specific surface area facilitate the exposure of active sites and can effectively increase the contact efficacy of ROS with PN-CeO_2, thus leading to high antioxidant activity. In addition, the surface properties of PN-CeO_2 were characterized by XPS. A Ce 3d scan at a binding energy of 870–920 kV validated the mixed oxidation state (Fig. 1(f)), showing a surface Ce^{3+} fraction of 32.7%. The large surface area and high surface Ce^{3+} fraction of PN-CeO_2 suggest its excellent ROS scavenging capability, indicating the potential of PN-CeO_2 as a reductive nanozyme against the protective autophagy that occurs during tumor reductive-damage therapy [49–55].

3.2 Antioxidative activities

The protective autophagy induced by over-generated ROS is critical for the development of a tumor [19, 20]. Thus, the catalytic activity of PN-CeO_2 for ROS-scavenging was assessed. Among the various biologically relevant ROS, H_2O_2 is one of the most important ROS because of its membrane permeability, longer half-life than that of $\cdot O_2^-$ and ·OH, and high intracellular dose [3]. Therefore, the CAT-like activity of PN-CeO_2 was initially evaluated using H_2O_2 as the substrate. As shown in Fig. 2(a), the CAT-like activity of PN-CeO_2 was observed in a dose-dependent manner, wherein the catalytic activity of PN-CeO_2 initially increased with an increase in the amount of catalyst and then reached saturation for H_2O_2 decomposition at a catalyst concentration of 50 μg/mL (Fig. 2(a)). Calibrated from the standard SOD assay kit, the PN-CeO_2 also exhibited SOD-like catalytic activity, significantly reducing the $\cdot O_2^-$ radicals. Similarly, the concentration-dependent SOD-like activity of the PN-CeO_2 was observed as shown in Fig. 2(b). When the concentration of PN-CeO_2 reached 50 μg/mL, the SOD-like activity of the PN-CeO_2 was saturated. In addition, the SOD-like activity of PN-CeO_2 was further confirmed by EPR spectroscopy (Fig. 2(c)). The catalytic performance of the PN-CeO_2 suggests its potential to achieve reductive-damage tumor therapy by scavenging excess ROS.

3.3 PN-CeO_2 as *in vitro* autophagy inhibitor

Firstly, the cellular uptake of PN-CeO_2 was examined by TEM. As shown in Fig. S1 in the Electronic Supplementary Material (ESM), the PN-CeO_2 particles were successfully taken up into the SCL-1 cells after 24 h of incubation. Then, to explore the potential effects of PN-CeO_2 on cell survival, SCL-1 cells were treated by PN-CeO_2 with various concentrations of 0, 5, 10, 25, 50, and 100 μg/mL for 24, 48, and 72 h. The MTT assay showed that PN-CeO_2 caused a significant inhibitory effect on SCL-1 cell growth in a time- and dose-dependent manner (Fig. 3(a)). Furthermore, to verify whether PN-CeO_2 was effective in other cancer cell types, the cytotoxicity on several common malignant tumor models was evaluated by MTT assay, including human cervical carcinoma cell line HeLa, colon cancer cell line HCT-116, prostate cancer cell line PC-3, lung adenocarcinoma cell line A549, and hepatocellular carcinoma cell line HepG2. As shown in Fig. S2 in the ESM, the results demonstrated that PN-CeO_2 had significant dose-dependent inhibitory effects on the growth of the tumor cells listed above, indicating the potential of PN-CeO_2 for the therapy of various tumors by catalytically inhibiting autophagy. The tumor cell viability assay is a key technique to elucidate the capability of a nanomedicine for anti-tumor therapy. The experimental results strongly suggest that the treatment of PN-CeO_2 at various concentrations delivers varying levels of cytotoxicity to the tumor cells, indicating the potential of PN-CeO_2 as an autophagy inhibitor for cancer treatment. Based on the above results, the doses (0, 50, and 100 μg/mL) and duration (48 h) of PN-CeO_2 treatment were selected as the standard procedure for subsequently studying the mechanism of research experiments.

HCQ, the only clinically approved autophagy inhibitor, was chosen for comparison with PN-CeO_2. SCL-1 cells were treated by PN-CeO_2 or HCQ with same concentrations of 0, 5, 10, and 25 μg/mL for 48 h. The MTT assay revealed that both PN-CeO_2 and HCQ significantly inhibited the growth of SCL-1 cells in a dose-dependent manner and HCQ appeared slightly more potent than PN-CeO_2 at the same dose (Fig. 3(b)). Given the potential toxicity of HCQ previously reported [29, 38, 39], the biosafety of PN-CeO_2 and HCQ was further compared using normal human keratinocytes (HaCaT). The influence of PN-CeO_2 and HCQ on HaCaT was evaluated by incubating nanozymes or HCQ at the aforementioned concentrations with the cells for 48 h. As shown in Fig. 3(c) and Fig. S3 in the ESM, PN-CeO_2 was non-toxic towards normal cell line HaCaT, even at a high concentration of 100 μg/mL. The viability of the cells was close to that of the control group, suggesting high biocompatibility of PN-CeO_2. However, the proliferation activity of the HaCaT cells in the HCQ-treated group was significantly reduced, suggesting a non-negligible toxicity of HCQ for normal cells at therapeutic dose. The comparisons showed that, at the same dose, the anti-tumor effect of HCQ was only 5.28%–12.47% higher than that of PN-CeO_2, but HCQ seriously affected the survival of normal cells (the survival rate was only 36.28% at the concentration of 25 μg/mL). These experimental results strongly suggest that, compared with highly toxic autophagy inhibitor, HCQ, PN-CeO_2 was demonstrated to be capable of autophagy inhibition and tumor treatment, with negligible side effects and satisfactory biocompatibility. The high biocompatibility of PN-CeO_2 can be explained by its thermodynamic stability under lysosomal acidifying conditions. Its dissolution rate decreases under acidifying conditions; therefore, it does not cause lysosomal damage, caspase 3 activation, pro-inflammatory production, or apoptotic cell death unlike other transition-metal oxides and rare-earth oxides [60].

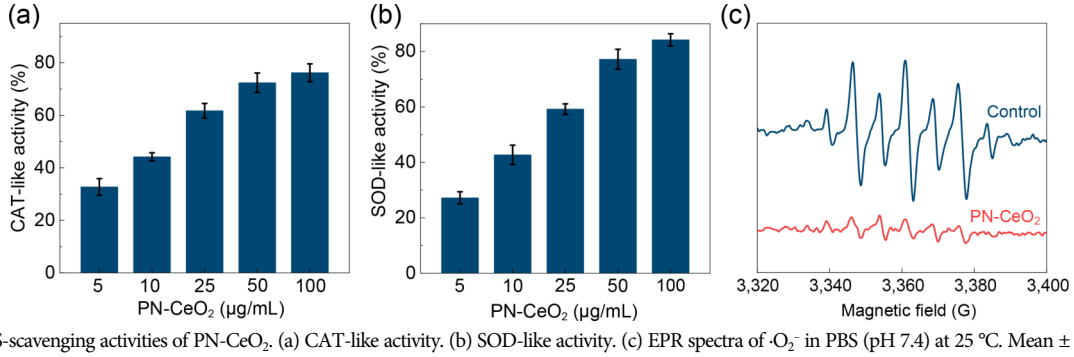

Figure 2 ROS-scavenging activities of PN-CeO_2. (a) CAT-like activity. (b) SOD-like activity. (c) EPR spectra of $\cdot O_2^-$ in PBS (pH 7.4) at 25 °C. Mean ± SEM, n = 3 per group.

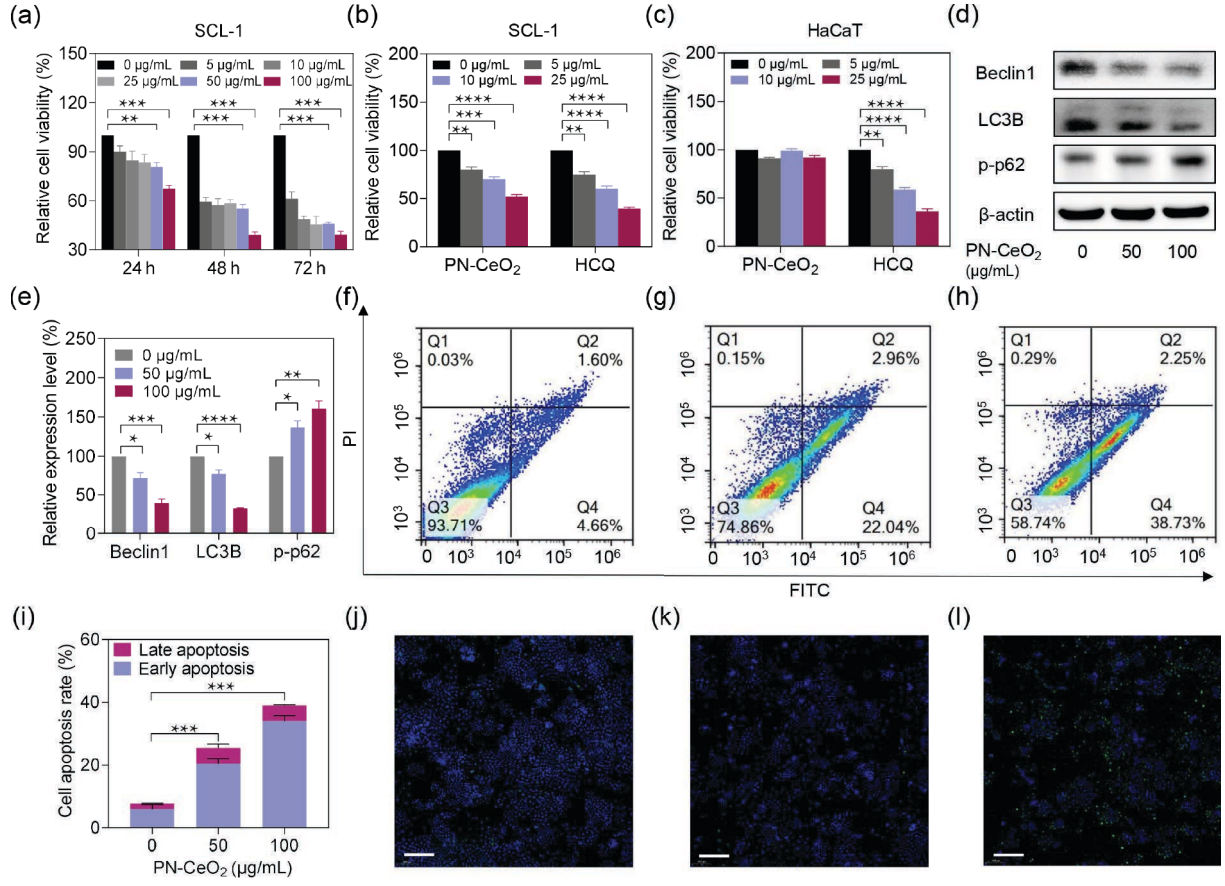

Figure 3 Anti-tumor effects of the PN-CeO_2 as an autophagy inhibitor in tumor cells. (a) Time- and dose-dependent cytotoxicity of PN-CeO_2 in SCL-1 cells. (b) Viability of SCL-1 cells treated with PN-CeO_2 and HCQ at indicated concentrations. (c) Viability of HaCaT cells treated with PN-CeO_2 and HCQ at different concentrations. (d) and (e) Western blot analyses of Beclin1, LC3B, and p-p62 in SCL-1 cells with different PN-CeO_2 treatments using β-actin as the internal control. (f)–(h) Flow cytometric apoptosis analysis of Annexin V-FITC/PI-stained SCL-1 cells after different PN-CeO_2 treatments: (f) 0, (g) 50, and (h) 100 μg/mL. (i) Quantitation of the apoptosis results with different treatments as indicated after 48h. (j)–(l) TUNEL staining for SCL-1 cells after different PN-CeO_2 treatments: (j) 0, (k) 50, and (l) 100 μg/mL. All scale bars are 200 μm. Mean ± SEM, $n = 3$ per group, $^*P < 0.05$, $^{**}P < 0.01$, $^{***}P < 0.001$, and $^{****}P < 0.0001$.

Accumulating evidence argues that oxidative stress and subsequent protective autophagy are critical for the development of a tumor [19, 20]. We speculate that PN-CeO_2, as an artificial antioxidant, can inhibit tumor growth by catalytically eliminating ROS, consequently reducing protective autophagy. Thus, the levels of autophagy in SCL-1 cells were evaluated after incubation with PN-CeO_2. As shown in Figs. 3(d) and 3(e), Beclin1, a hallmark of autophagy involved in the early-stage of autophagy initiation and a phagophore assembly, and microtubule-associated protein 1 LC3B [61], a typical autophagosome marker associated with post-translational modifications followed by the formation of autophagosomes, were downregulated after 48 h of treatment with PN-CeO_2. This demonstrates a significant inhibitory effect imposed by PN-CeO_2 on autophagy in skin tumors. Generally, the inhibition of autophagy is accompanied by the prominent accumulation of p62 and p-p62 [62]. As shown in Figs. 3(d) and 3(e), the increased p-p62 accumulation in SCL-1 cells suggests the inhibition of autophagy by PN-CeO_2. The above results confirm that PN-CeO_2 is an effective autophagy inhibitor that lowers the level of autophagy in tumor cells.

Considering the relationship between apoptosis and autophagy, the apoptosis rates of SCL-1 cells with different concentrations of PN-CeO_2 for 48 h were investigated by flow cytometry using an Annexin V-FITC/PI kit. After incubation with PN-CeO_2 as the autophagy inhibitor, increased levels of apoptosis were observed (Figs. 3(f)–3(i)). Untreated cells showed a relatively low basal apoptosis rate of 7.78% in SCL-1 cells, while treatment with PN-CeO_2 induced a significant increase in cellular apoptosis in a dose-dependent manner (Fig. 3(i)). Furthermore, the TUNEL assay demonstrated higher apoptosis rates and lower cell counts in the PN-CeO_2-treated groups relative to those in the quality control group, suggesting that apoptosis was the main mechanism of cell death mediated by PN-CeO_2 (Figs. 3(j)–3(l)). Autophagy, as a predominantly cytoprotective mechanism, can degrade impaired organelles, particularly mitochondria, to prevent subsequent apoptosis and support the survival of cancer cells [21–24]. The increased levels of autophagy in tumor cells are thus closely linked to apoptosis inhibition. In turn, a lack of autophagy can activate apoptosis and induce cell death [31, 32]. Our results showed that PN-CeO_2, as an artificial autophagy inhibitor, significantly increased apoptosis in skin tumor cells, further demonstrating the efficient tumor-suppressing function of PN-CeO_2.

3.4 Mechanisms of autophagy inhibition by PN-CeO_2

It is widely believed that ROS scavenging efficaciously blocks pro-survival autophagy and has been identified as a promising strategy for reductive-damage therapy in advanced cancers [25, 33–36]. To verify whether PN-CeO_2 could induce reductive damage to achieve autophagy inhibition, the reduction capacity of PN-CeO_2 was examined at a high intracellular ROS level within tumor cells. The SCL-1 cells were stained with DCFH-DA for the fluorescence detection of intracellular ROS by confocal laser scanning microscopy. As shown in Figs. 4(a) and 4(b), the tumor cells without any treatment displayed relatively strong green fluorescence, while cells incubated with PN-CeO_2 exhibited significant decrease in the levels of the intracellular ROS in a dose-dependent manner, demonstrating the ROS-scavenging ability of PN-CeO_2. Furthermore, the quantitative analyses of the ROS levels

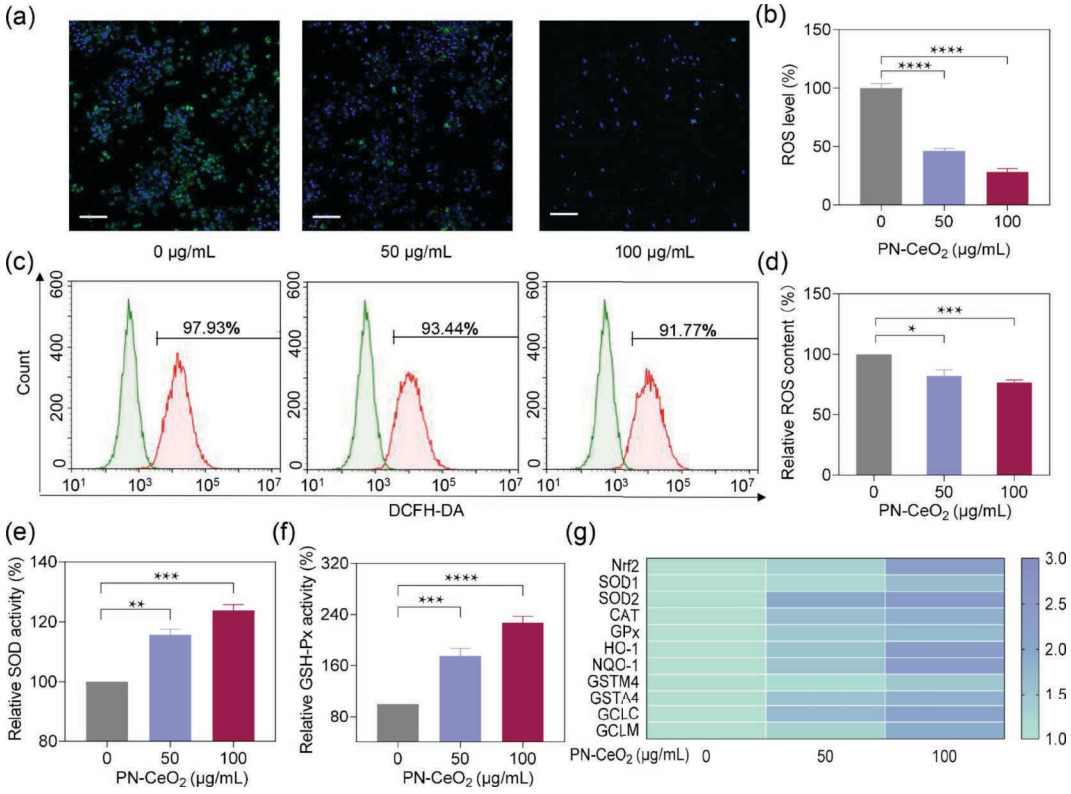

Figure 4 ROS degradation efficiency of PN-CeO_2 in tumor cells. (a) Fluorescent images of SCL-1 cells after co-incubation with PN-CeO_2 for 48 h and subsequent staining with the ROS fluorescence probe DCFH-DA (all scale bars are 100 μm). (b) Intracellular ROS levels in SCL-1 cells incubated with PN-CeO_2 for 48 h. (c) Flow cytometric ROS analysis of DCFH-DA-stained SCL-1 cells after different PN-CeO_2 treatments (0, 50, and 100 μg/mL). (d) Quantitation of ROS results. (e) SOD and (f) GSH-Px levels in SCL-1 cells. (g) PN-CeO_2-induced antioxidant enzymes through Nrf2 pathway activation. mRNA levels of Nrf2, SOD1, SOD2, CAT, GPx, HO-1, NQO-1, GSTM1, GSTA4, GCLC, and GCLM in SCL-1 cells treated with PN-CeO_2 (0, 50, and 100 μg/mL) for 48 h. Mean ± SEM, $n = 3$ per group, $^*P < 0.05$, $^{**}P < 0.01$, $^{***}P < 0.001$, and $^{****}P < 0.0001$.

of SCL-1 cells under various treatments were examined by flow cytometry. The ROS levels of the cells treated with PN-CeO_2 at concentrations of 50 and 100 μg/mL decreased to 82.0% and 76.6% of those in the untreated cells, respectively (Figs. 4(c) and 4(d)).

Based on increasing knowledge of cancer biology and its altered redox status, researchers have explored numerous tumor therapy strategies, including chemotherapy, radiotherapy, photodynamic therapy, and chemodynamic therapy [1–18]. Most of these tend to enhance the generation of intracellular or exogenous ROS and interfere with antioxidant defenses. The significant downside of these ROS-inducing therapy strategies is the toxic effects on normal and healthy cells, tissues, and normal organs [2]. In addition, long term application of chemotherapy and other ROS-producing methods cause tumor cells to become resistant to the increase of exogenous ROS, seriously affecting their therapeutic efficacy [2, 4]. In contrast, ROS scavenging in tumor treatment will not cause the above issues, and thus reductive damage therapy seems an apt strategy to abrogate ROS-mediated cellular processes and inhibit cancers. Interestingly, we demonstrated that the potent anti-tumor therapeutic effects of PN-CeO_2 were mediated by ROS scavenging, not overproduction, which is a vital supplement to the anti-tumor effects of existing nanomaterials.

Given the enzyme-mimicking activities of nanoceria, the levels of SOD and GSH-Px, the most important antioxidases in animals, were also examined. After PN-CeO_2 treatment for 48 h, the SOD and GSH-Px levels significantly increased because of the antioxidant activity of PN-CeO_2 (Figs. 4(e) and 4(f)). Specifically, the intracellular SOD and GSH-Px levels increased by 23.86% and 127%, respectively, when the cells were treated with 100 μg/mL of PN-CeO_2. These results indicate that PN-CeO_2 exhibits SOD-mimetic activity catalytically converting superoxide anions into H_2O_2, which further detoxifies into H_2O and O_2 through the CAT-mimetic activity. Therefore, the high capability of PN-CeO_2 to inhibit ROS accumulation in cSCC cells demonstrates its potential as a powerful autophagy inhibitor for reductive-damage tumor therapy via ROS scavenging.

The capability of PN-CeO_2 as an autophagy inhibitor for the induced mRNA expression of antioxidases in SCL-1 cells was further examined by qRT-PCR (Fig. 4(g)). Compared with the control group, the expression of antioxidases, including SOD, CAT, GSH-Px, HO-1, and NQO-1, was significantly increased in the PN-CeO_2-treated groups. The expression of their upstream regulatory gene, Nrf2, was also upregulated upon PN-CeO_2 treatment (Figs. 4(g), 5(a), and 5(b)). Nrf2 represents one of the most important endogenous mechanisms for resisting persistent oxidative stress in cells [51]. Previously, the interplay between autophagy and Nrf2-Kelch-like ECH-associated protein 1 (Keap1) system demonstrated that autophagy substrate p-p62 was responsible for the release of Nrf2 from the Nrf2-Keap1 complex and Nrf2 nuclear translocation, thereby inducing the expression of downstream antioxidant genes such as SOD, GSH-Px, HO-1, and NQO-1 [63, 64]. Thus, p-p62 accumulation related to deficient autophagy may account for the abovementioned upregulation of Nrf2 levels and the expression of many downstream antioxidant genes after PN-CeO_2 treatment (Figs. 3(d), 3(e), 4(g), 5(a), and 5(b)). This highlights that, in addition to antioxidant enzyme-mimicking activities, PN-CeO_2 also reduces ROS by inhibiting autophagy and activating the Nrf2-mediated antioxidant pathway, thereby forming a positive feedback reductive-damage cycle to achieve sufficient autophagy inhibition.

A few common ROS-activated mechanistic pathways upregulate autophagy in cancer cells, including the AMP-activated protein kinase, PI3K/AKT, and p38 MAPK pathways [58, 59].

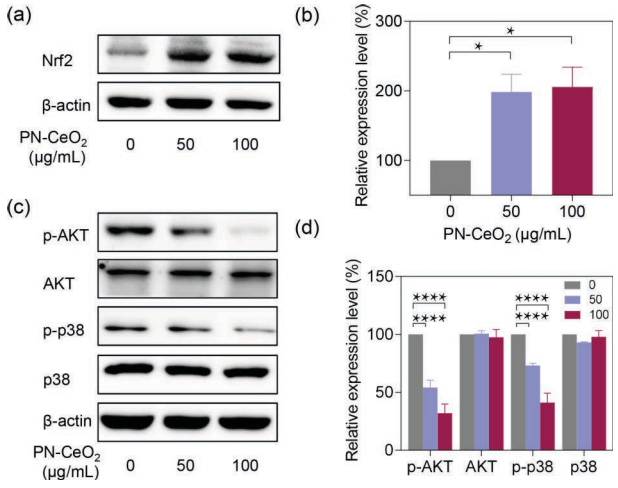

Figure 5 Effects of PN-CeO_2 on ROS-associated signaling pathways. (a) and (b) Western blot analyses of Nrf2 in SCL-1 cells with different PN-CeO_2 treatments after 48 h using β-actin as an internal control. (c) and (d) Western blot analyses of p-AKT, AKT, p-p38, and p38 in SCL-1 cells with different PN-CeO_2 treatments using β-actin as an internal control. Mean ± SEM, n = 3 per group, $^*P < 0.05$, and $^{****}P < 0.0001$.

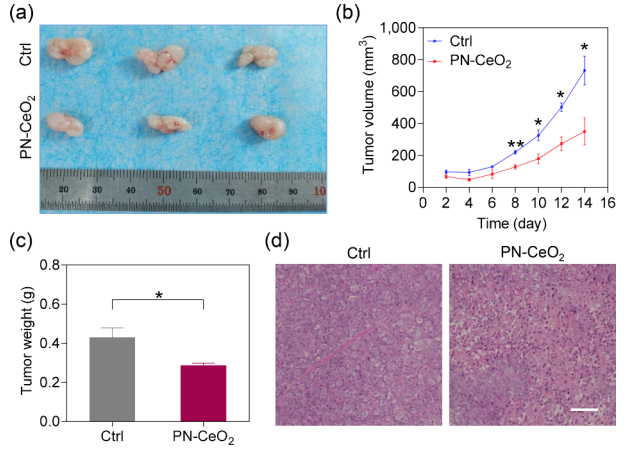

Figure 6 The antineoplastic effects of PN-CeO_2 *in vivo*. (a) Photographs of dissected tumors after 12 days of treatment. (b) Relative tumor volumes of SCL-1-bearing nude mice intravenously injected (tail vein) with catalysts and saline (control group). (c) Tumor weights after 12 days of treatment. (d) H&E staining for pathological changes in tumor tissues. Scale bar is 100 μm. Mean ± SEM, n = 3 per group, $^*P < 0.05$, and $^{**}P < 0.01$.

Hence, the protein expression in these autophagy-related signal pathways was evaluated for cells treated with PN-CeO_2. PN-CeO_2 inhibited the activities of the PI3K/AKT and p38 MAPK pathways, as illustrated by the reduced levels of phospho-AKT and phospho-p38 (Figs. 5(c) and 5(d)). Our results indicate that the catalytic ability of PN-CeO_2 to reduce of ROS levels plays a critical role upstream of the PI3K/AKT and p38 MAPK signaling pathways. This confirms that PN-CeO_2-enabled autophagy-inhibition and the subsequent anti-tumor effects on SCL-1 cells by the reductive-damage strategy are mediated by the abrogation of the PI3K/AKT and p38 MAPK signaling pathways. The results of these *in vitro* experiments demonstrate the effectiveness of this reductive-damage strategy in mediating autophagy inhibition for tumor treatment at the cellular level owing to the scavenging of ROS and the enhancement of the inherent antioxidant defenses of tumor cells.

3.5 *In vivo* ROS-reduction-mediated anti-tumor activity of PN-CeO_2 as an autophagy inhibitor

After realizing the inhibitory effects of PN-CeO_2 on the autophagy of cSCC cells, *in vivo* experiments were carried out on a mouse xenograft model of cutaneous squamous cell carcinoma. Tumor cells were subcutaneously implanted into the right flanks of female BALB/c/nu nude mice. Then, 0.1 mL of 0.9% saline (control) or PN-CeO_2 (10 mg/kg/mouse) was intravenously administered to the mouse xenograft models before 12 days observation. Consistent with the results of the *in vitro* experiments, the administration of PN-CeO_2 inhibited the *in vivo* tumor growth in the treated group as compared with that of the untreated group (Fig. 6(a)). Compared with the control group, the tumors from the PN-CeO_2-treated group exhibited significantly smaller sizes and much lower weights without any apparent decrease in body weight, demonstrating the therapeutic capacity and biological safety of the PN-CeO_2 *in vivo* (Figs. 6(b) and 6(c), and Fig. S4 in the ESM). In addition, the PN-CeO_2 treatment against tumors was evaluated by H&E staining, which revealed significant tumor necrosis and apoptosis in the PN-CeO_2-treated mice (Fig. 6(d)).

The autophagy-inhibition activity of PN-CeO_2 was also examined in the xenograft tumor models (Figs. 7(a)–7(d)). Compared with that of the control group, PN-CeO_2 significantly downregulated Beclin1 and LC3B and up-regulated p-p62 expression *in vivo*, which was highly consistent with the *in vitro* autophagy-suppression effects (Figs. 3(d) and 3(e)). The ROS levels of the tumors were significantly lower in the PN-CeO_2-treated group than those in the control group (Figs. 7(e) and 7(f)). Similar to the *in vitro* results (Figs. 4(e) and 4(f)), the increased activity of intratumoral antioxidant enzymes, including SOD and GSH-Px, played a crucial role in this process (Fig. 7(g)). Moreover, the xenografts treated with PN-CeO_2 exhibited a greater increase in positive TUNEL staining than those in the control group, further validating the tumor-inhibition performance of PN-CeO_2 (Fig. 7(h)). Immunofluorescence images of Caspase3, the most important protein in the apoptotic pathway, revealed the apparent apoptosis of the tumor tissue in the PN-CeO_2-treated group (Figs. 7(d) and 7(i)). Regarding the autophagy-related signal pathways, the levels of phospho-AKT and phospho-p38 in the tumor tissues were examined using immunofluorescent staining [58, 59]. As shown in Figs. 7(j) and 7(k), compared with that of the control group, the group treated with PN-CeO_2 exhibited significantly downregulated p-AKT and p-p38 expression *in vivo*, consistent with the *in vitro* results (Figs. 5(c) and 5(d)). This high consistency between *in vivo* and *in vitro* results strongly suggests that a single intravenous injection of PN-CeO_2 (10 mg/kg/mouse) is sufficient to effectively scavenge ROS and inhibit autophagy in a xenograft tumor model.

After administration, PN-CeO_2 was primarily distributed in the livers and spleens of the SCL-1-tumor-bearing mice and presented a substantial decline over time (determined by ICP-MS, Figs. S5 and S6 in the ESM), illustrating the high biocompatibility and safety of PN-CeO_2 as an autophagy inhibitor [52, 65]. In addition, PN-CeO_2 effectively accumulated within tumor tissues after injection, indicating the high bioavailability of PN-CeO_2 for tumor treatment (Fig. S5 in the ESM). Furthermore, cerium was detected in the urine and feces, indicating the metabolism of PN-CeO_2 and further demonstrating its biosafety (Fig. S6 in the ESM). The H&E staining of major organs (heart, liver, spleen, lung, and kidney) and blood biochemical indices, including alanine aminotransferase, aspartate aminotransferase, alkaline phosphatase, albumin, blood urea nitrogen, and creatinine, were assessed to evaluate the adverse side effects of PN-CeO_2. H&E staining revealed no obvious destructive cell necrosis or inflammatory lesions in the major organs (Fig. S7 in the ESM) and no significant change in liver and kidney function in the treated group as compared with the control group (Fig. S8 in the ESM), reinforcing the high biocompatibility and safety of PN-CeO_2 [66]. The above data clearly demonstrate the validity of using PN-CeO_2 as a reductive-damage strategy for tumor therapy. PN-CeO_2 can

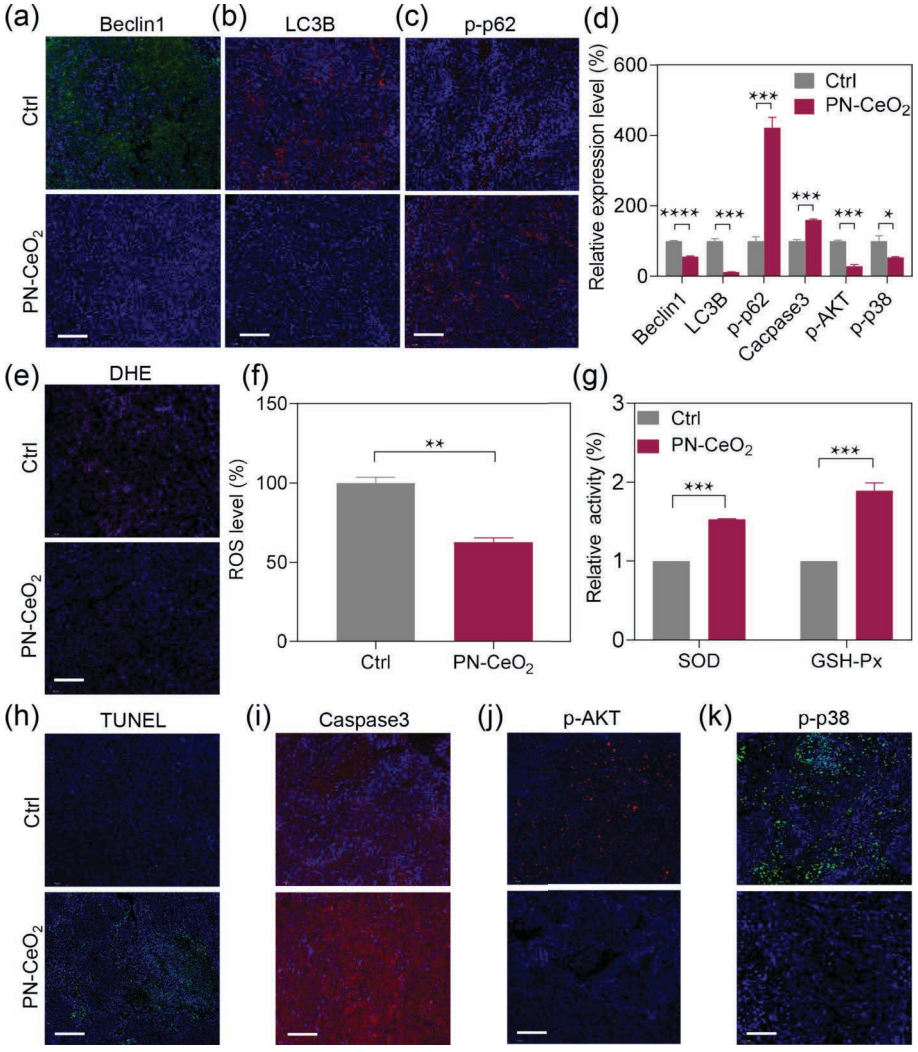

Figure 7 *In vivo* reductive-damage of PN-CeO_2 as an autophagy inhibitor. (a)–(c) Fluorescent images of Beclin1-, LC3B-, and p-p62-stained tumor tissues after 12 days of treatment. (d) Relative expression levels of Beclin1, LC3B, p-p62, caspase-3, p-AKT, and p-p38 in tumor tissues with and without PN-CeO_2 treatments. (e) and (f) ROS staining and quantitative analysis of ROS levels in tumor tissues after different treatment. (g) SOD and GSH-Px levels in tumor tissues after 12 days of treatment. (h) and (i) TUNEL staining and fluorescent images of Caspase-3 staining of tumor tissues after PN-CeO_2 treatment. (j) and (k) Fluorescent images of p-AKT- and p-p38-stained tumor tissues after treatment. All scale bars are 100 μm. Mean ± SEM, $n = 3$ per group, $^*P < 0.05$, $^{**}P < 0.01$, $^{***}P < 0.001$, and $^{****}P < 0.0001$.

act as a promising artificial autophagy inhibitor to deliver significant anti-tumor efficacy *in vivo* by the ROS-modulated downregulation of autophagy with negligible adverse effects.

4 Conclusions

In summary, we demonstrated that PN-CeO_2, as an artificial autophagy inhibitor, significantly suppressed the proliferation and tumor growth of human cSCC by inhibiting autophagy and promoting apoptosis through a reductive-damage strategy, which was mediated by a catalytic downregulation of the ROS-related pathway for tumor treatment. The extensive control experiments revealed the catalytic reductive-damage pathway of PN-CeO_2 as an autophagy inhibitor with anti-tumor capabilities. In addition, negligible adverse effects were noted both *in vitro* and *in vivo*, implying the high biocompatibility and safety of PN-CeO_2. Since overproduced ROS and autophagy survival are hallmarks of an extensive range of tumors, this unique reductive-damage strategy of scavenging ROS rather than increasing it is anticipated to be a promising alternative for the treatment and management of tumors.

Acknowledgements

We thank Professor Yi Lv and his colleague from the National Local Joint Engineering Research Center for Precision Surgery and Regenerative Medicine, Shaanxi Province Center for Regenerative Medicine and Surgery Engineering Research. This work was supported by grants from the National Natural Science Foundation of China (Nos. 81972938, 52002314, and 21872109) and partially supported by Funds of Shaanxi Province (Nos. 2021ZDLSF03-01, 2020TD-043, and TZ0124), General Project of Shaanxi Natural Science Basic Research Plan (No. 2021JM-589), and Xi'an People's Hospital (Xi'an Fourth Hospital) Research Incubation Fund Project (LH-1). The authors also acknowledge the support from the Fundamental Research Funds for the Central Universities (Nos. D5000210829 and G2021KY05102).

Electronic Supplementary Material: Supplementary material (cellular uptake of PN-CeO_2, effects of PN-CeO_2 on several common malignant tumor models, viability of HaCaT cells treated with PN-CeO_2 at different concentrations, time-dependent body-weight curves of SCL-1 tumor-bearing nude mice, the biodistribution of Ce element in main tissues and tumors after injection of PN-CeO_2, measurement of Ce element concentration in urine and feces samples, H&E-stained images of main organs, and measurement of liver and kidney function in mice after different treatment) is available in the online version of this article at https://doi.org/10.1007/s12274-022-5139-z.

References

[1] Helleday, T. Poisoning cancer cells with oxidized nucleosides. *N. Engl. J. Med.* **2015**, *373*, 1570–1571.

[2] Perillo, B.; Di Donato, M.; Pezone, A.; Di Zazzo, E.; Giovannelli, P.; Galasso, G.; Castoria, G.; Migliaccio, A. ROS in cancer therapy: The bright side of the moon. *Exp. Mol. Med.* **2020**, *52*, 192–203.

[3] Galadari, S.; Rahman, A.; Pallichankandy, S.; Thayyullathil, F. Reactive oxygen species and cancer paradox: To promote or to suppress? *Free Radic. Biol. Med.* **2017**, *104*, 144–164.

[4] Yang, H. T.; Villani, R. M.; Wang, H. L.; Simpson, M. J.; Roberts, M. S.; Tang, M.; Liang, X. W. The role of cellular reactive oxygen species in cancer chemotherapy. *J. Exp. Clin. Cancer Res.* **2018**, *37*, 266.

[5] Liu, C.; Lin, Q.; Yun, Z. Cellular and molecular mechanisms underlying oxygen-dependent radiosensitivity. *Radiat. Res.* **2015**, *183*, 487–496.

[6] Pham, T. C.; Nguyen, V. N.; Choi, Y.; Lee, S.; Yoon, J. Recent strategies to develop innovative photosensitizers for enhanced photodynamic therapy. *Chem. Rev.* **2021**, *121*, 13454–13619.

[7] He, G. L.; Xu, N.; Ge, H. Y.; Lu, Y.; Wang, R.; Wang, H. X.; Du, J. J.; Fan, J. L.; Sun, W.; Peng, X. J. Red-light-responsive Ru complex photosensitizer for lysosome localization photodynamic therapy. *ACS Appl. Mater. Interfaces* **2021**, *13*, 19572–19580.

[8] Yang, B. W.; Chen, Y.; Shi, J. L. Reactive oxygen species (ROS)-based nanomedicine. *Chem. Rev.* **2019**, *119*, 4881–4985.

[9] Chen, J. J.; Zhu, Y. F.; Wu, C. T.; Shi, J. L. Nanoplatform-based cascade engineering for cancer therapy. *Chem. Soc. Rev.* **2020**, *49*, 9057–9094.

[10] Canaparo, R.; Foglietta, F.; Limongi, T.; Serpe, L. Biomedical applications of reactive oxygen species generation by metal nanoparticles. *Materials (Basel)* **2021**, *14*, 53.

[11] Wang, X. W.; Zhong, X. Y.; Liu, Z.; Cheng, L. Recent progress of chemodynamic therapy-induced combination cancer therapy. *Nano Today* **2020**, *35*, 100946.

[12] He, Y. X.; Liu, S. H.; Yin, J.; Yoon, J. Sonodynamic and chemodynamic therapy based on organic/organometallic sensitizers. *Coord. Chem. Rev.* **2021**, *429*, 213610.

[13] Zhang, C. Y.; Wang, X.; Du, J. F.; Gu, Z. J.; Zhao, Y. L. Reactive oxygen species-regulating strategies based on nanomaterials for disease treatment. *Adv. Sci.* **2021**, *8*, 2002797.

[14] Wang, X. Q.; Wang, W. J.; Peng, M. Y.; Zhang, X. Z. Free radicals for cancer theranostics. *Biomaterials* **2021**, *266*, 120474.

[15] Fan, W. P.; Yung, B.; Huang, P.; Chen, X. Y. Nanotechnology for multimodal synergistic cancer therapy. *Chem. Rev.* **2017**, *117*, 13566–13638.

[16] Yang, J. Y.; Zhao, Y.; Zhou, Y. Y.; Wei, X. L.; Wang, H. J.; Si, N.; Yang, J.; Zhao, Q. H.; Bian, B. L.; Zhao, H. Y. Advanced nanomedicines for the regulation of cancer metabolism. *Biomaterials* **2022**, *286*, 121565.

[17] Wang, M.; Chang, M. Y.; Li, C. X.; Chen, Q.; Hou, Z. Y.; Xing, B. G.; Lin, J. Tumor-microenvironment-activated reactive oxygen species amplifier for enzymatic cascade cancer starvation/chemodynamic/immunotherapy. *Adv. Mater.* **2022**, *34*, 2106010.

[18] Zhang, X. H.; Guo, R. C.; Chen, Y. F.; Xu, X.; Yang, Z. X.; Cheng, D. B.; Chen, H.; Qiao, Z. Y.; Wang, H. A BiOCl nanodevice for pancreatic tumor imaging and mitochondria-targeted therapy. *Nano Today* **2021**, *40*, 101285.

[19] Filomeni, G.; De Zio, D.; Cecconi, F. Oxidative stress and autophagy: The clash between damage and metabolic needs. *Cell. Death. Differ.* **2015**, *22*, 377–388.

[20] Xia, H. J.; Green, D. R.; Zou, W. P. Autophagy in tumour immunity and therapy. *Nat. Rev. Cancer* **2021**, *21*, 281–297.

[21] Doherty, J.; Baehrecke, E. H. Life, death and autophagy. *Nat. Cell Biol.* **2018**, *20*, 1110–1117.

[22] Huang, J.; Brumell, J. H. Bacteria-autophagy interplay: A battle for survival. *Nat. Rev. Microbiol.* **2014**, *12*, 101–114.

[23] Galluzzi, L.; Green, D. R. Autophagy-independent functions of the autophagy machinery. *Cell* **2019**, *177*, 1682–1699.

[24] Stukalov, A.; Girault, V.; Grass, V.; Karayel, O.; Bergant, V.; Urban, C.; Haas, D. A.; Huang, Y. Q.; Oubraham, L.; Wang, A. Q. et al. Multilevel proteomics reveals host perturbations by SARS-CoV-2 and SARS-CoV. *Nature* **2021**, *594*, 246–252.

[25] Yamazaki, T.; Pedro, J. M. B. S.; Galluzzi, L.; Kroemer, G.; Pietrocola, F. Autophagy in the cancer-immunity dialogue. *Adv. Drug Deliv. Rev.* **2021**, *169*, 40–50.

[26] Wang, L.; Wang, Y. T.; Zhao, W.; Lin, K. L.; Li, W.; Wang, G. D.; Zhang, Q. Library screening to identify highly-effective autophagy inhibitors for improving photothermal cancer therapy. *Nano Lett.* **2021**, *21*, 9476–9484.

[27] Gao, G.; Sun, X. B.; Liu, X. Y.; Jiang, Y. W.; Tang, R. Q.; Guo, Y. X.; Wu, F. G.; Liang, G. L. Intracellular nanoparticle formation and hydroxychloroquine release for autophagy-inhibited mild-temperature photothermal therapy for tumors. *Adv. Funct. Mater.* **2021**, *31*, 2102832.

[28] Wang, X. H.; Li, M.; Ren, K. B.; Xia, C. Y.; Li, J. P.; Yu, Q. W.; Qiu, Y.; Lu, Z. Z.; Long, Y.; Zhang, Z. R. et al. On-demand autophagy cascade amplification nanoparticles precisely enhanced oxaliplatin-induced cancer immunotherapy. *Adv. Mater.* **2020**, *32*, 2002160.

[29] Xie, Y. X.; Jiang, J. N.; Tang, Q. Y.; Zou, H. B.; Zhao, X.; Liu, H. M.; Ma, D.; Cai, C. L.; Zhou, Y.; Chen, X. J. et al. Iron oxide nanoparticles as autophagy intervention agents suppress hepatoma growth by enhancing tumoricidal autophagy. *Adv. Sci.* **2020**, *7*, 1903323.

[30] Shashni, B.; Nagasaki, Y. Nitroxide radical-containing nanoparticles attenuate tumorigenic potential of triple negative breast cancer. *Biomaterials* **2018**, *178*, 48–62.

[31] Wang, J. F.; Zhou, X. F.; Wang, H. F.; Xiao, Q.; Ding, K. F.; Dong, X.; Xu, S. F.; Shen, B.; Sun, J. H.; Zhou, Z. X. et al. Autophagy-inhibiting polymer as an effective nonviral cancer gene therapy vector with inherent apoptosis-sensitizing ability. *Biomaterials* **2020**, *255*, 120156.

[32] Kim, K. Y.; Park, K. I.; Kim, S. H.; Yu, S. N.; Park, S. G.; Kim, Y. W.; Seo, Y. K.; Ma, J. Y.; Ahn, S. C. Inhibition of autophagy promotes salinomycin-induced apoptosis via reactive oxygen species-mediated PI3K/AKT/mTOR and ERK/p38 MAPK-dependent signaling in human prostate cancer cells. *Int. J. Mol. Sci.* **2017**, *18*, 1088.

[33] Xu, J.; Wang, H. S.; Hu, Y.; Zhang, Y. S.; Wen, L. P.; Yin, F.; Wang, Z. Y.; Zhang, Y. C.; Li, S. Y.; Miao, Y. Y. et al. Inhibition of CaMKIIα activity enhances antitumor effect of fullerene C60 nanocrystals by suppression of autophagic degradation. *Adv. Sci.* **2019**, *6*, 1801233.

[34] Wei, W. J.; Rosenkrans, Z. T.; Luo, Q. Y.; Lan, X. L.; Cai, W. B. Exploiting nanomaterial-mediated autophagy for cancer therapy. *Small Methods* **2019**, *3*, 1800365.

[35] Chen, M. L.; Yang, D.; Sun, Y.; Liu, T.; Wang, W. H.; Fu, J. T.; Wang, Q. Q.; Bai, X. Q.; Quan, G. L.; Pan, X. et al. *In situ* self-assembly nanomicelle microneedles for enhanced photoimmunotherapy via autophagy regulation strategy. *ACS Nano* **2021**, *15*, 3387–3401.

[36] Li, F. L.; Chen, T.; Wang, F.; Chen, J. F.; Zhang, Y. Y.; Song, D. T.; Li, N.; Lin, X. H.; Lin, L. S.; Zhuang, J. Y. Enhanced cancer starvation therapy enabled by an autophagy inhibitors-encapsulated biomimetic ZIF-8 nanodrug: Disrupting and harnessing dual pro-survival autophagic responses. *ACS Appl. Mater. Interfaces* **2022**, *14*, 21860–21871.

[37] Wang, M.; Chen, Q.; Xu, D.; Yang, Z. B.; Chen, J. F.; Zhang, Y.; Chen, H. R. Self-cycling redox nanoplatform in synergy with mild magnetothermal and autophagy inhibition for efficient cancer therapy. *Nano Today* **2022**, *43*, 101374.

[38] Schrezenmeier, E.; Dörner, T. Mechanisms of action of hydroxychloroquine and chloroquine: Implications for rheumatology. *Nat. Rev. Rheumatol.* **2020**, *16*, 155–166.

[39] Ruan, S. B.; Xie, R.; Qin, L.; Yu, M. N.; Xiao, W.; Hu, C.; Yu, W. Q.; Qian, Z. Y.; Ouyang, L.; He, Q. et al. Aggregable nanoparticles-enabled chemotherapy and autophagy inhibition combined with anti-PD-L1 antibody for improved glioma treatment. *Nano Lett.* **2019**, *19*, 8318–8332.

[40] Shen, W. T.; Zhang, X. Y.; Fu, X.; Fan, J. J.; Luan, J. Y.; Cao, Z. L.;

Yang, P.; Xu, Z. Y.; Ju, D. W. A novel and promising therapeutic approach for NSCLC: Recombinant human arginase alone or combined with autophagy inhibitor. *Cell Death Dis.* **2017**, *8*, e2720.

[41] Bellare, G. P.; Patro, B. S. Resveratrol sensitizes breast cancer to PARP inhibitor, talazoparib through dual inhibition of AKT and autophagy flux. *Biochem. Pharmacol.* **2022**, *199*, 115024.

[42] Wang, Q.; Cheng, C. Q.; Zhao, S.; Liu, Q. Y.; Zhang, Y. H.; Liu, W. L.; Zhao, X. Z.; Zhang, H.; Pu, J.; Zhang, S. et al. A valence-engineered self-cascading antioxidant nanozyme for the therapy of inflammatory bowel disease. *Angew. Chem., Int. Ed.* **2022**, *61*, e202201101.

[43] Wang, L. Y.; Zhu, B. H.; Deng, Y. T.; Li, T. T.; Tian, Q. Y.; Yuan, Z. G.; Ma, L.; Cheng, C.; Guo, Q. Y.; Qiu, L. Biocatalytic and antioxidant nanostructures for ROS scavenging and biotherapeutics. *Adv. Funct. Mater.* **2021**, *31*, 2101804.

[44] Wu, J. J.; Wang, X. Y.; Wang, Q.; Lou, Z. P.; Li, S. R.; Zhu, Y. Y.; Qin, L.; Wei, H. Nanomaterials with enzyme-like characteristics (nanozymes): Next-generation artificial enzymes(II). *Chem. Soc. Rev.* **2019**, *48*, 1004–1076.

[45] Wang, H.; Wan, K. W.; Shi, X. H. Recent advances in nanozyme research. *Adv. Mater.* **2019**, *31*, 1805368.

[46] Huang, Y. Y.; Ren, J. S.; Qu, X. G. Nanozymes: Classification, catalytic mechanisms, activity regulation, and applications. *Chem. Rev.* **2019**, *119*, 4357–4412.

[47] Jiang, D. W.; Ni, D. L.; Rosenkrans, Z. T.; Huang, P.; Yan, X. Y.; Cai, W. B. Nanozyme: New horizons for responsive biomedical applications. *Chem. Soc. Rev.* **2019**, *48*, 3683–3704.

[48] Tang, G. H.; He, J. Y.; Liu, J. W.; Yan, X. Y.; Fan, K. L. Nanozyme for tumor therapy: Surface modification matters. *Exploration* **2021**, *1*, 75–89.

[49] Zhao, S.; Li, Y. X.; Liu, Q. Y.; Li, S. R.; Cheng, Y.; Cheng, C. Q.; Sun, Z. Y.; Du, Y.; Butch, C. J.; Wei, H. An orally administered CeO_2@montmorillonite nanozyme targets inflammation for inflammatory bowel disease therapy. *Adv. Funct. Mater.* **2020**, *30*, 2004692.

[50] Tian, Z. M.; Li, X. H.; Ma, Y. Y.; Chen, T.; Xu, D. H.; Wang, B. C.; Qu, Y. Q.; Gao, Y. Quantitatively intrinsic biomimetic catalytic activity of nanocerias as radical scavengers and their ability against H_2O_2 and doxorubicin-induced oxidative stress. *ACS Appl. Mater. Interfaces* **2017**, *9*, 23342–23352.

[51] Weng, Q. J.; Sun, H.; Fang, C. Y.; Xia, F.; Liao, H. W.; Lee, J.; Wang, J. C.; Xie, A.; Ren, J. F.; Guo, X. et al. Catalytic activity tunable ceria nanoparticles prevent chemotherapy-induced acute kidney injury without interference with chemotherapeutics. *Nat. Commun.* **2021**, *12*, 1436.

[52] Tian, Z. M.; Zhao, J. L.; Zhao, S. J.; Li, H. C.; Guo, Z. X.; Liang, Z. C.; Li, J. Y.; Qu, Y. Q.; Chen, D. F.; Liu, L. Phytic acid-modified CeO_2 as Ca^{2+} inhibitor for a security reversal of tumor drug resistance. *Nano Res.* **2022**, *15*, 4334–4343.

[53] Naha, P. C.; Hsu, J. C.; Kim, J.; Shah, S.; Bouché, M.; Si-Mohamed, S.; Rosario-Berrios, D. N.; Douek, P.; Hajfathalian, M.; Yasini, P. et al. Dextran-coated cerium oxide nanoparticles: A computed tomography contrast agent for imaging the gastrointestinal tract and inflammatory bowel disease. *ACS Nano* **2020**, *14*, 10187–10197.

[54] Soh, M.; Kang, D. W.; Jeong, H. G.; Kim, D.; Kim, D. Y.; Yang, W.; Song, C.; Baik, S.; Choi, I. Y.; Ki, S. K. et al. Ceria-zirconia nanoparticles as an enhanced multi-antioxidant for sepsis treatment. *Angew. Chem., Int. Ed.* **2017**, *56*, 11399–11403.

[55] Karakoti, A.; Singh, S.; Dowding, J. M.; Seal, S.; Self, W. T. Redox-active radical scavenging nanomaterials. *Chem. Soc. Rev.* **2010**, *39*, 4422–4432.

[56] Boey, A.; Leong, S. Q.; Bhave, S.; Ho, H. K. Cerium oxide nanoparticles alleviate hepatic fibrosis phenotypes *in vitro*. *Int. J. Mol. Sci.* **2021**, *22*, 11777.

[57] Global Burden of Disease 2019 Cancer Collaboration. Cancer incidence, mortality, years of life lost, years lived with disability, and disability-adjusted life years for 29 cancer groups from 2010 to 2019: A systematic analysis for the global burden of disease study 2019. *JAMA Oncol.* **2022**, *8*, 420–444.

[58] White, E. Deconvoluting the context-dependent role for autophagy in cancer. *Nat. Rev. Cancer* **2012**, *12*, 401–410.

[59] Chae, Y. C.; Vaira, V.; Caino, M. C.; Tang, H. Y.; Seo, J. H.; Kossenkov, A. V.; Ottobrini, L.; Martelli, C.; Lucignani, G.; Bertolini, I. et al. Mitochondrial Akt regulation of hypoxic tumor reprogramming. *Cancer Cell* **2016**, *30*, 257–272.

[60] Mirshafiee, V.; Sun, B. B.; Chang, C. H.; Liao, Y. P.; Jiang, W.; Jiang, J. H.; Liu, X. S.; Wang, X.; Xia, T.; Nel, A. E. Toxicological profiling of metal oxide nanoparticles in liver context reveals pyroptosis in Kupffer cells and macrophages versus apoptosis in hepatocytes. *ACS Nano* **2018**, *12*, 3836–3852.

[61] Levine, B.; Kroemer, G. Biological functions of autophagy genes: A disease perspective. *Cell* **2019**, *176*, 11–42.

[62] Moscat, J.; Karin, M.; Diaz-Meco, M. T. p62 in cancer: Signaling adaptor beyond autophagy. *Cell* **2016**, *167*, 606–609.

[63] Yang, B. W.; Ding, L.; Yao, H. L.; Chen, Y.; Shi, J. L. A metal-organic framework (MOF) Fenton nanoagent-enabled nanocatalytic cancer therapy in synergy with autophagy inhibition. *Adv. Mater.* **2020**, *32*, 1907152.

[64] Jang, J.; Wang, Y. D.; Lalli, M. A.; Guzman, E.; Godshalk, S. E.; Zhou, H. J.; Kosik, K. S. Primary cilium-autophagy-Nrf2 (PAN) axis activation commits human embryonic stem cells to a neuroectoderm fate. *Cell* **2016**, *165*, 410–420.

[65] Tai, W. Y.; Li, J. W.; Corey, E.; Gao, X. H. A ribonucleoprotein octamer for targeted siRNA delivery. *Nat. Biomed. Eng.* **2018**, *2*, 326–337.

[66] Chen, L. J.; Jiang, X. W.; Lv, M.; Wang, X. L.; Zhao, P. R.; Zhang, M.; Lv, G. L.; Wu, J. Y.; Liu, Y. Y.; Yang, Y. et al. Reductive-damage-induced intracellular maladaptation for cancer electronic interference therapy. *Chem* **2022**, *8*, 866–879.